

On the Importance of Spatial Resolution for Flap Side Edge Noise Prediction

Raymond E. Mineck*
Yorktown, Virginia 23692

and

Mehdi R. Khorrami†
NASA Langley Research Center, Hampton, Virginia, 23681

A spatial resolution study of flap tip flow and the effects on the farfield noise signature for an 18%-scale, semispan Gulfstream aircraft model are presented. The NASA FUN3D unstructured, compressible Navier-Stokes solver was used to perform the highly resolved, time-dependent, detached eddy simulations of the flow field associated with the flap for this high-fidelity aircraft model. Following our previous work on the same model, the latest computations were undertaken to determine the causes of deficiencies observed in our earlier predictions of the steady and unsteady surface pressures and off-surface flow field at the flap tip regions, in particular the outboard tip area, where the presence of a cavity at the side-edge produces very complex flow features and interactions. The present results show gradual improvement in steady loading at the outboard flap edge region with increasing spatial resolution, yielding more accurate fluctuating surface pressures, off-surface flow field, and farfield noise with improved high-frequency content when compared with wind tunnel measurements. The spatial resolution trends observed in the present study demonstrate that the deficiencies reported in our previous computations are mostly caused by inadequate spatial resolution and are not related to the turbulence model.

Nomenclature

| | | |
|-------------------|---|---|
| C_p | = | average of the time history of the pressure coefficient |
| Hz | = | Hertz, cycles per second |
| PSD | = | power spectral density in psi^2/Hz |
| psi | = | pounds per square inch |
| p_{tavg} | = | time average of the static pressure |
| X, Y, Z | = | right handed coordinate system |

I. Introduction

Mitigation of aircraft noise is a critical goal of the NASA Aeronautics Research Mission Directorate. Airframe noise constitutes a major component of the total aircraft noise during approach and landing. Previous flight test campaigns¹⁻⁶ and model-scale tests⁷⁻⁸ in ground facilities have identified wing high-lift devices and aircraft landing gear as the primary sources of airframe noise. As major components of a high-lift system, flaps, in particular flap tip regions, are prominent noise generators. Accurate prediction of flap tip noise requires careful consideration of the highly complex, unsteady flow field produced by air that separates at the edges.

An experimental study of a realistic flap system as installed on an 18% scale, semispan replica of a Gulfstream aircraft was conducted to elucidate flow behavior in the tip region and its effect on farfield noise. Data acquired from extensive testing⁹⁻¹³ of the model were used to validate the complementary computational simulations¹⁴⁻¹⁶ conducted with the Exa Corporation PowerFLOW® Lattice-Boltzmann solver and the NASA FUN3D solver. The latter, a standard unstructured grid, compressible Navier-Stokes solver was used by Khorrami and Mineck¹⁵ (herein after referred to as KM) to perform delayed detached eddy simulations (DDES) of the aircraft model. Although KM's results captured some of the relevant flow features associated with the model's complex flap, several noticeable deficiencies at the tip regions emerged. The most glaring was failure to predict the steady and unsteady surface

* Consultant

† Aerospace Engineer, Computational AeroSciences Branch, Associate Fellow AIAA

pressures at the flap outboard edge. As a result, the predicted farfield noise spectrum displayed a rapid roll off around 6 kHz and lacked a key tonal feature. In KM, the observed deficiencies were conjectured to be caused by insufficient spatial resolution, inability or inadequacy of the turbulence model to capture the complex unsteady three-dimensional flow, or a combination of both.

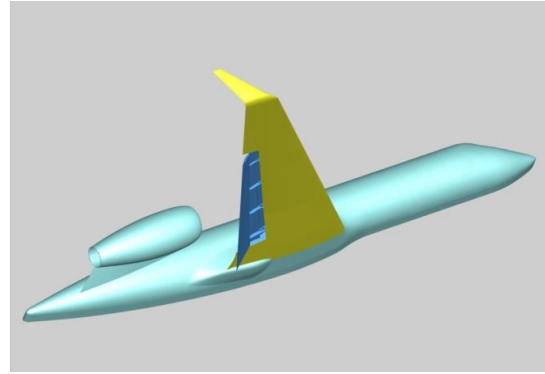
In an attempt to remedy some of the shortcomings observed in KM and to determine which effect is the key factor, we have conducted additional simulations using grids with improved spatial resolution in the vicinity of the aircraft model flap. Gains in solution accuracy and their effect on steady and unsteady surface pressures and farfield noise signature are presented and discussed in this paper.

II. Simulated Model Geometry

Following KM, the simulated model geometry corresponds to an 18% scale, semispan, high-fidelity reproduction of a Gulfstream aircraft that was tested in the NASA Langley Research Center (LaRC) 14- by 22-Foot (14x22) Subsonic Tunnel (see Fig. 1). The complete model geometry consists of a fuselage, wing, flap, flow-through nacelle, pylon, and main landing gear. A full description of this model, including instrumentation, is provided in Refs. 9 and 10. Since the present effort was focused on the flap flow field, the main landing gear was omitted from the simulations. Figure 2 shows a top view of the wing and flap, including the spanwise location and numbering of the static pressure rows used in this study.

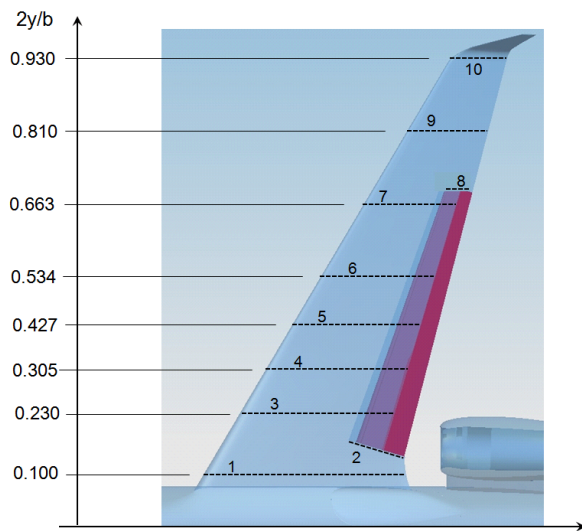


a) Installed in the NASA LaRC 14x22 tunnel

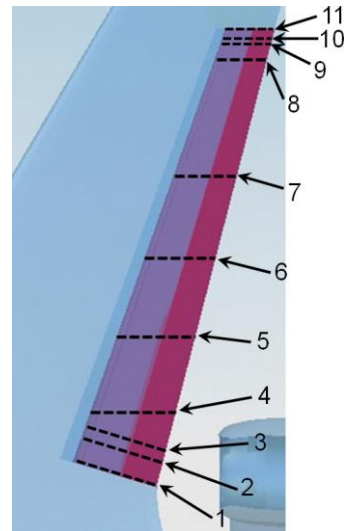


b) CAD model

Figure 1. 18% -scale semispan model of a Gulfstream aircraft.



a) Wing



b) Flap

Figure 2. Spanwise location and numbering for rows of static pressure orifices on wing and flap.

Altogether, the flap has 40 dynamic sensors distributed in three distinct areas: along the midspan section, subsequently referred to as the main body of the flap, and two narrow, chordwise strips adjacent to the inboard and outboard edges where significant flow unsteadiness is expected. Figure 3, taken from Ref. 10, displays the locations and numbering of the unsteady pressure sensors near the inboard and outboard side-edges of the model flap used for comparison with the present computations. Note that the flap outboard side-edge has a cavity that nearly spans the entire chord length. In the actual aircraft, this cavity houses a bulb seal that prevents metal-to-metal contact during flap retraction. To capture the cavity surface pressure fluctuations at high flap deflections, two probes (P26 and P27) were installed inside the cavity. The simulated geometry includes the cavity and bulb seal as tested during the 14x22 wind tunnel experiments.

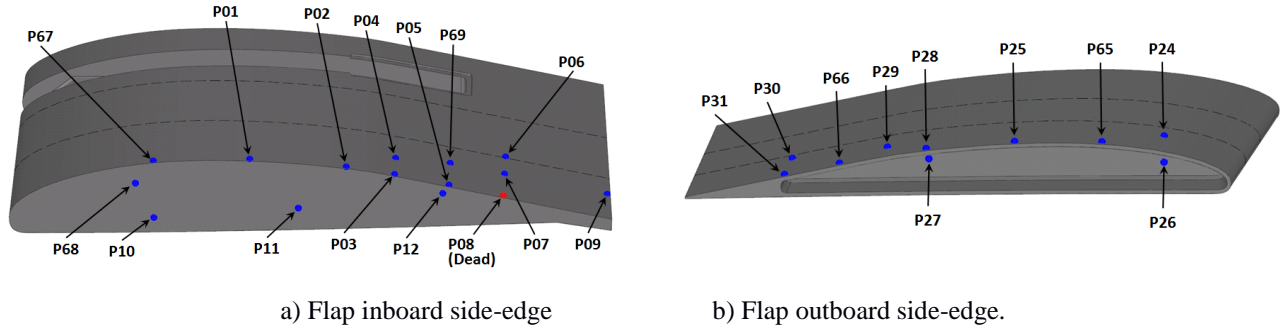


Figure 3. Locations and numbering of probes (transducers) installed at the flap side-edges (Ref. 10).

III. Computational Approach

The numerical approach used in the present work is identical to that outlined in KM and Vatsa et al.¹⁶ For completeness, we present a brief summary of the key aspects of the computational procedure. For more information, the reader should consult Refs. 15 – 17.

A. Flow Solver

The NASA LaRC spatially second-order accurate CFD solver FUN3D was used to perform the simulations. FUN3D uses finite-volume discretization to solve either the steady or time-dependent compressible Reynolds-Averaged Navier-Stokes (RANS) equations at the nodes of unstructured grids. The equations can be converged to a steady state or solved in time-accurate mode. Variable time steps at each node are used to accelerate convergence for steady flows. A constant time step at each node is used for unsteady flows (time-accurate mode). For steady flows, the solution at each time step is updated with a backward Euler time differencing scheme and the use of local time stepping. At each time step, the linear system of equations is relaxed in a red-black fashion with a point-implicit algorithm. For time-accurate simulations, time is advanced using a second-order, backward difference approach. Various types of grid elements ranging from tetrahedrons, pyramids, and prisms, to hexahedrons, can be accommodated in the computational mesh. Multiple inviscid upwind flux functions, gradient limiters, and boundary conditions are available. The computational domain is decomposed with MPI communications to allow distributed computing on multiple computer nodes.

B. Turbulence Models

For steady calculations, the simulations were conducted using the one-equation Spalart-Allmaras (SA) model¹⁸ in conjunction with the solid-body rotation modification of Dacles-Mariani et al.¹⁹ As in the KM study, following Vatsa et al.,^{16,17} a hybrid approach based on the RANS equations with the SA model¹⁸ near the wall and a modified version of the Delayed Detached Eddy Simulation (DDES) model (MDDES) in the rest of the computational domain was used to perform the unsteady computations.

C. Computational Grids

The axis system for the computational grids was aligned with the vehicle body axes (X along the line from the nose to the tail, Y from the centerline to the right wing tip, and Z pointing away from the ground, a right-handed axis system). Locations and distances are presented in nondimensional grid units with a length scale of one inch (0.0254m). The nose of the fuselage was located at (-0.72, -3.50, 13.95), the end of the fuselage at (184.68, -3.50, 20.37), and the tip of the winglet at (146.11, 100.82, 23.86). The computational domain was a semicylinder with the inflow boundary at X=-569.42, the outflow boundary at X=1145.23, and the far field at a radius of 616.00 with the origin at Y=-3.75. The viscous floor was embedded within the reflection plane. The viscous floor extended in the X direction from about -130 to about 329 and in the Z direction from about 132 to -105.

Three computational grids were used in this study. The grid referred to as Grid 14 enriched in KM was selected as baseline. Two grid refinements were performed sequentially, referred to as Grid 14 enriched 2 and Grid 14 enriched 3. The new grids were generated to obtain values of y^+ less than 1, refined node spacing in regions with significant pressure gradients, and refined node spacing in close proximity of the flap side edges. Additional refinements were added to the region in the vicinity of the flap top surface to better resolve the confluent shear flows generated by the interaction between the main wing wake and the flow jetting through the flap gap. The grids were designed to simulate the model in the open test section (free-air setup). Based on results from Ref. 16, mixed element grids were used to achieve better numerical accuracy.

The baseline grid (Grid 14 enriched) used in KM was generated in three steps. The NASA TetrUSS suite²⁰ was used to create the surface mesh and a volume grid with only tetrahedral elements. The volume grid was converted to mixed elements (tetrahedrons, pyramids, and prisms) using Pointwise[®] grid generation software.²¹ This grid included a relatively large region with refined node spacing beneath the wing and flap to allow direct extraction of the radiating acoustic waves and comparisons with the predicted values from a Ffowcs-Williams Hawking (FWH) propagation code (Figs. 11 and 12 from Ref. 15). A close-up view of the simulated cutout (cavity) in the outboard side-edge of the flap including the bulb seal is shown in Fig. 4. The surface mesh near the flap outboard side-edge extracted from our finest grid (Grid 14 enriched 3) is presented in Fig. 5.

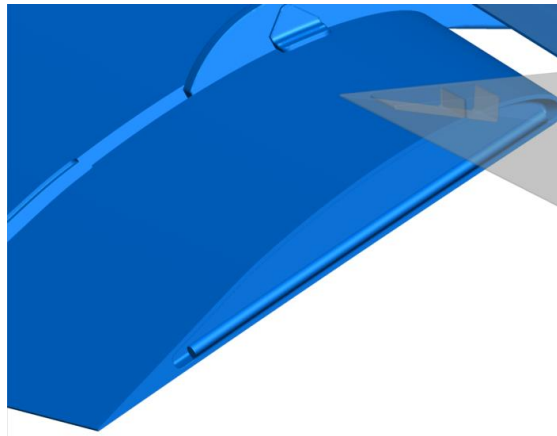


Figure 4. Close up view of model geometry near flap outboard tip.

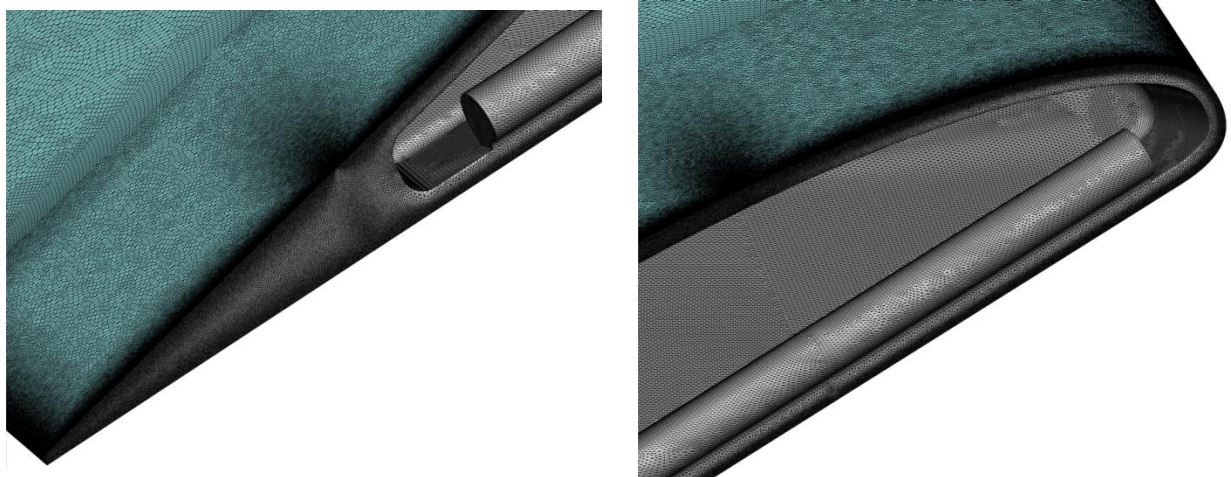


Figure 5. Close up view of computational mesh near flap outboard tip for Grid 14 enriched 3.

The Grid 14 enriched 2 grid was generated in 2 steps. TetrUSS was used to generate the surface mesh. The region of refined node spacing below the wing and flap was eliminated because comparisons of direct computations with the FWH analysis were no longer needed. This significantly reduced the number of tetrahedra and thus the computational

resources required to complete the simulation. Node spacing on the upper and lower surfaces of the flap, as well as on the inboard and outboard side-edges of the flap, was reduced to about 40% of that used for the baseline grid. Pointwise® software was used to create the mixed element volume grid.

Grid 14 enriched 3 was generated in like manner. Node spacing for the surface was further reduced near the inboard and outboard side-edges of the flap. Node spacing was also reduced in the volume mesh near the flap side-edges and above the flap along the path of the tip vortices. Grid characteristics for all three grids are listed in the table below.

Table 1. Grid attributes of the three grids used in the present study.

| Number of: (in millions) | Grid 14 enriched | Grid 14 enriched 2 | Grid 14 enriched 3 |
|-------------------------------------|-------------------------|---------------------------|---------------------------|
| nodes | 233.1 | 184.0 | 357.2 |
| tetrahedra | 976.8 | 698.3 | 1,287.2 |
| pyramids | 0.5 | 0.6 | 1.96 |
| prisms | 131.2 | 133.3 | 281.4 |

D. Boundary Conditions

All vehicle surfaces and the floor region near the model were simulated with no-slip boundary conditions. The remaining portion of the floor was modeled as a reflection plane. The inflow, outflow, and farfield boundary conditions were based on the Riemann invariants.

E. Computational Procedure

FUN3D was initially run in steady mode starting from freestream conditions with 500 first-order iterations to quickly establish the general flow field. The CFL number was ramped linearly over 200 iterations from 1 to 25 for the flow solver and from 1 to 5 for the turbulence equation. The inviscid flux construction used Roe's scheme with no limiter. The SA turbulence model¹⁸ with Dacles-Mariani modification¹⁹ was used for the steady calculations. The steady equations were run for about 5000 iterations, at which point the integrated force and moment coefficients were starting to settle within a reasonable band. The code was then run in time accurate mode, with 14 subiterations per time step, using the MDES turbulence model. A time step (Δt) of 2.499×10^{-6} seconds was used for the current simulations, providing a temporal resolution of 20 time steps per 20 kHz wave. Averaging of the flow variables in the entire volume commenced after the time-accurate simulation was run for 5000 time steps to allow the initial transients to die out. Thereafter, for all three grids, the pressure at each dynamic sensor location was recorded at each time step. For grids 14 enriched and 14 enriched 3, the pressure at each viscous surface node was recorded at each time step as well for farfield noise prediction.

For Grid 14 enriched, 106k time steps were used to obtain the averaged surface pressure coefficient distributions at the locations of the static pressure orifices on the wing and flap, as well as on planes of constant X near the flap inboard and outboard side edges. The surface pressure record at each dynamic sensor location obtained during the last 74k time steps was divided into smaller blocks and processed to obtain an averaged PSD distribution in psi^2/Hz . The analysis was applied to 17 blocks of 8k time steps, with each block having a 50% overlap with the previous block. The FWH approach used surface pressure data obtained during the last 45k time steps to yield the predicted pressure history at the farfield point specified in the wind tunnel tests. The initial 6567 time steps were discarded to allow the signal from all the surface pressure locations to propagate to this farfield point. The resulting pressure history was processed to obtain the PSD distribution in dB/Hz for an average over 9 blocks of 7.5k time steps.

For Grid 14 enriched 2, 40k time steps were used to obtain the averaged surface pressure distributions. For this grid, the simulation and processing of the data were stopped early (hence shorter time records) because the computations were not producing the expected improvements in pressure distribution near the outboard side edge of the flap. The pressure history at the dynamic sensor locations was obtained for the last 34k time steps. These results were processed in the same manner as those for the enriched grid for PSD distribution over 8 overlapping blocks of 8k time steps. No surface pressure data for use with the FWH propagation code were recorded for this grid.

For Grid 14 enriched 3, 71k time steps were used to obtain the averaged surface pressure distributions at the locations of the static pressure orifices on the wing and flap, as well as cutting planes near the flap side edges. The pressure histories at the dynamic sensor locations were obtained for the same 71k time steps. These results were processed to obtain the averaged PSD distribution over 16 overlapping blocks of 8k time steps each. The surface

pressure data for the FWH analysis used the last 70k time steps. As before, the initial 6567 time steps were discarded to allow the signal from all the surface pressure locations to propagate to the farfield point. The resulting pressure history was processed to obtain the PSD distribution in dB/Hz for an average over 17 blocks of 7.5k time steps.

IV. Results and Discussion

During the second 14x22 wind tunnel entry,¹¹⁻¹² aerodynamic and acoustic measurements of the 18% semispan model were obtained with the tunnel in the open-wall (open-jet) configuration. All the simulations were performed for a free-air condition that models the open-wall tunnel condition, an angle of attack of 3°, flap deflection angle of 39° (landing configuration), and with the main landing gear removed.

As mentioned in section III.C, the computations in FUN3D were performed in a nondimensional fashion. The scales used in our normalizations are the freestream speed of sound, density, kinematic viscosity, and a unit length of 1.0 inch (0.0254m). For the present case, reference flow variables were set to match conditions at the 14x22 tunnel test section entrance. All simulations were obtained for a freestream Mach number of 0.2. The corresponding Reynolds number is 1.33 million per foot (4.40 million per meter), resulting in a value of 3.40 million based on the 18% model mean aerodynamic chord of 30.8 in (0.782 m). Because both upper and lower surfaces of the wing were tripped in the experiment,⁹ the computations were conducted in fully turbulent mode.

A. Global View

Figure 6a shows the averaged time-accurate surface pressure distribution over the semispan model with its flap deployed. The displayed contours are from our previous simulation for Grid 14 enriched presented in KM. The surface pressures display the footprint of a strong suction peak at the inboard edge, attributed to the presence of strong streamwise vortices. In contrast, the outboard edge lacks a similar suction peak, indicating that either the edge vortices are not properly resolved or that the chosen turbulence model falls short of properly capturing the complicated flow interactions. The effects of increased spatial resolution on the surface pressure distributions at the inboard edge were minor; thus, they will not be shown. At the outboard edge, depicted in detail in Fig. 6b, the increase in spatial resolution gradually enhances the suction levels inside the tip cavity and a narrow strip adjacent to the edge, defining a more prominent footprint of the vortical flow at the tip.

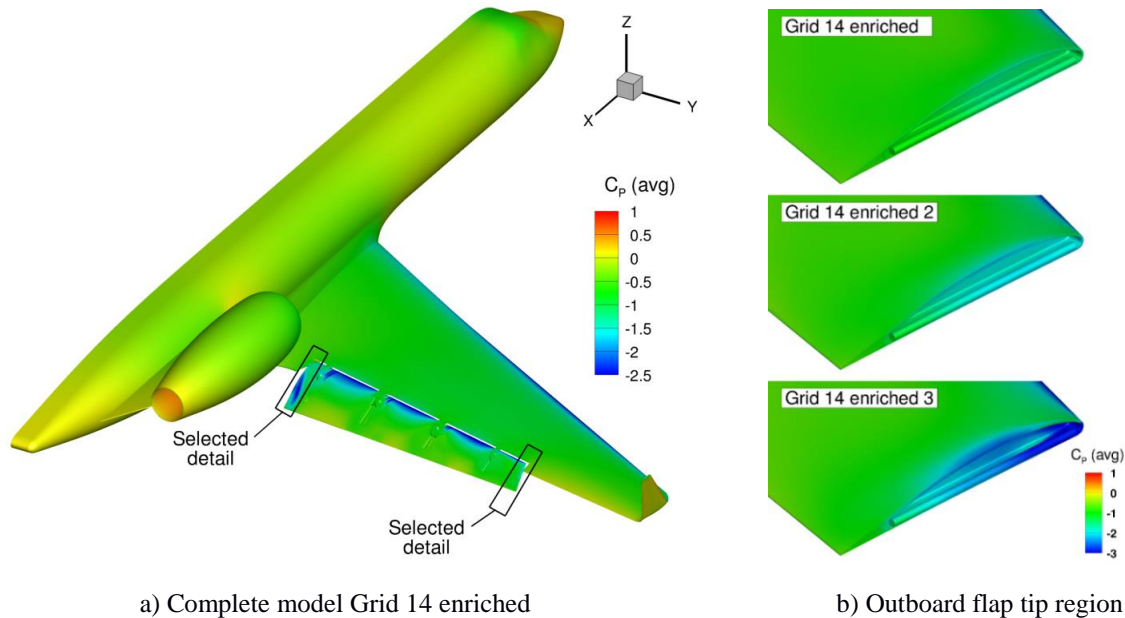


Figure 6. Computed average of the time-accurate surface pressure distributions on the 18%-scale model.

A comparison of the time-averaged, nondimensional, off-surface pressure contours near the flap inboard and outboard side-edges at several streamwise stations is presented in Figs. 7 and 8 for Grid 14 enriched and Grid 14 enriched 3. At the inboard edge (Fig. 7), although both grids capture the formation and merging of the dual vortex system, contours from Grid 14 enriched 3 show slightly greater detail in the flow features as a result of refined node spacing. The improvement due to grid refinement is substantial at the outboard side-edge (Fig. 8), where much stronger vortex-cavity interaction and tip vortex emerge. Notice the significant increase in the pressure range obtained with

Grid 14 enriched 3 as compared to the grid used in our earlier study, resulting in a much stronger tip vortex with a low pressure core that lingers beyond the flap trailing edge.

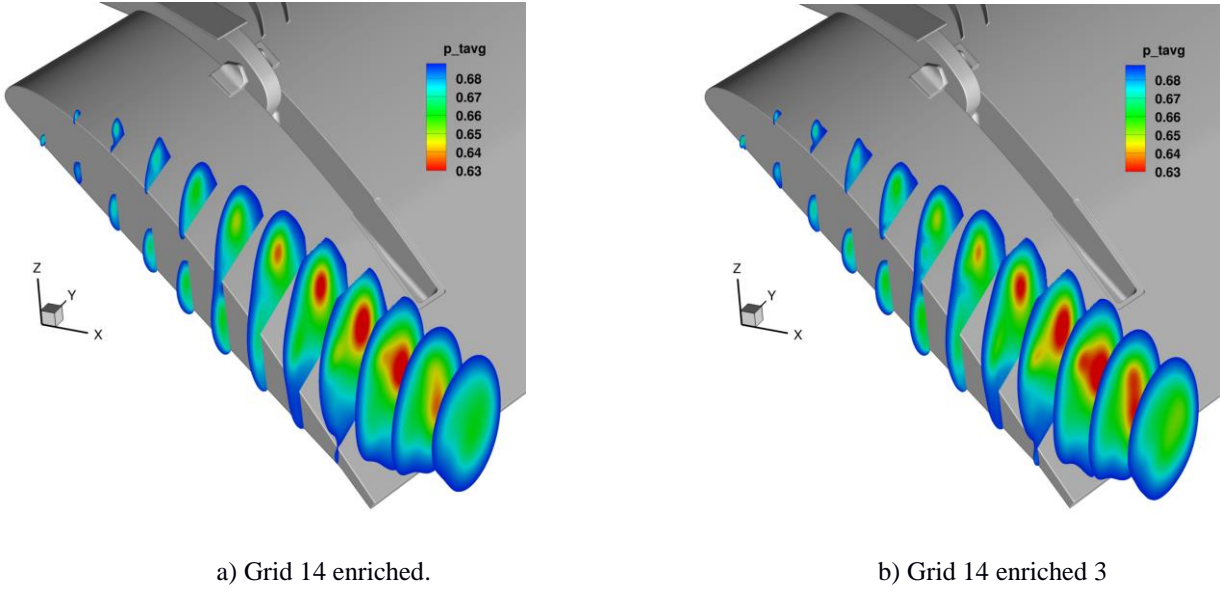


Figure 7. Average static pressure contours at the inboard flap side-edge highlighting the formation of a dual vortex system and location of vortex cores.

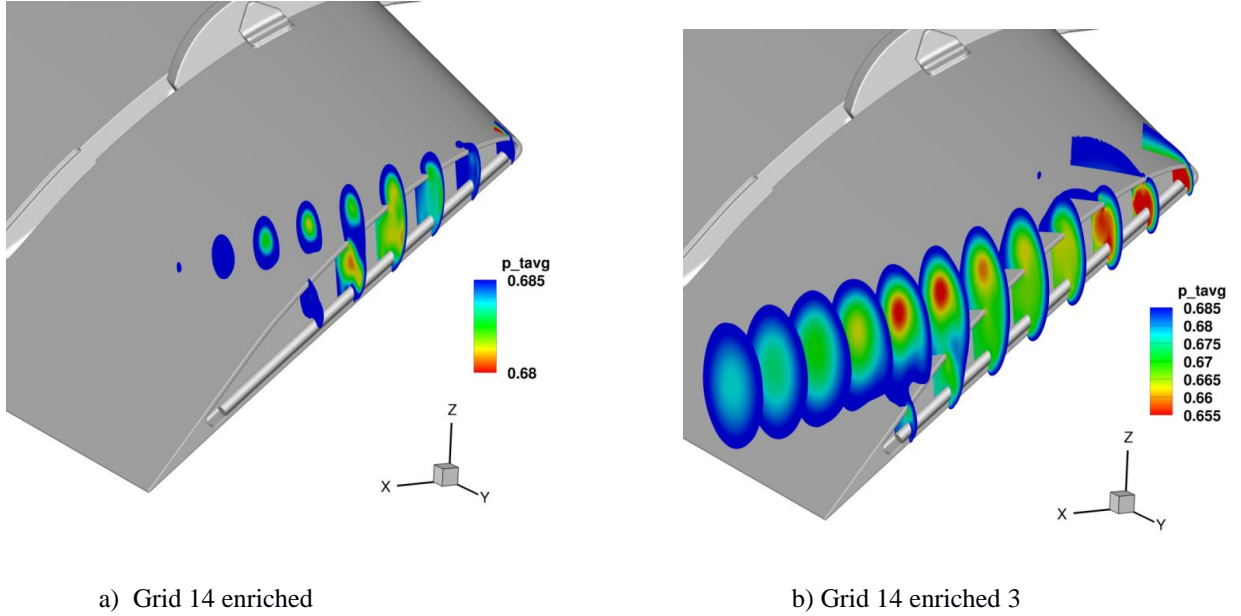


Figure 8. Average static pressure contours at the outboard flap side-edge, highlighting vortex-cavity interaction and location of vortex cores.

B. Surface Pressure Coefficient (C_p)

The computed time-averaged C_p distributions on the wing for all three grids were found to be in good agreement with measured pressure values. As a sample plot, presented in Fig. 9a is the pressure distribution at wing row 5. Note that the distributions are nearly identical, as expected, since the refinements had a minimal effect on the mesh near the wing. Similarly, computed time-averaged C_p distributions at the midsection of the flap (rows 5-7 in Fig. 2b) were

found to be in good agreement with measured values. Presented in Fig. 9b is a sample plot for row 6, corresponding to the flap midspan.

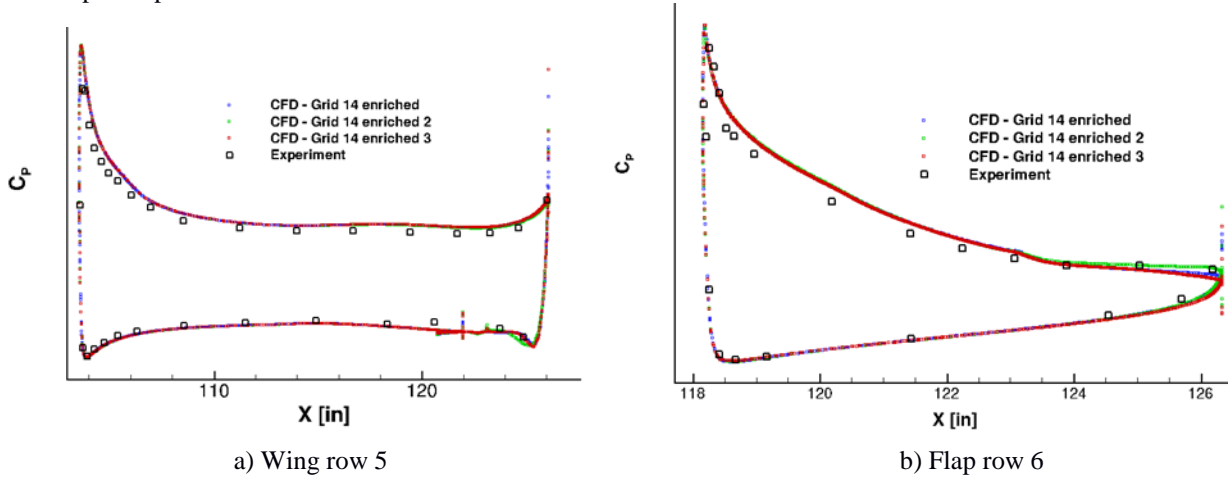


Figure 9. Averaged time-accurate surface pressure distribution at wing row 5 and flap row 6.

The flow unsteadiness generated by a deflected flap occurs mostly in the vicinity of the two side edges. Computed time-averaged C_p distributions at the four orifice rows closest to the flap inboard edge are plotted in Fig. 10. Overall, there is good agreement between the three computed solutions and the measured values, with Grid 14 enriched 3 results displaying subtle improvement (e.g., Fig. 10a). Comparison of the pressure distributions at the inboard edge indicates that Grid 14 enriched provided sufficient resolution to capture the local vortical flow.

Pressure distributions at the rows closest to the flap outboard side edge are plotted in Fig. 11. As can be seen from the figures, there is gradual improvement in the computed solution with increased spatial resolution that is consistent with the contour plots shown in Figs. 6b and 8b. The most significant gain is attained at row 11 (Fig. 11d), which is adjacent to the edge and captures the surface pressure footprint of the tip vortex. Nevertheless, even the very fine Grid 14 enriched 3 seems to be insufficient for capturing the local suction peak at $X = 128$ in., as well as the main suction region aft of $X = 129.5$ in. that is produced by the tip primary vortex migrating to the flap upper surface.

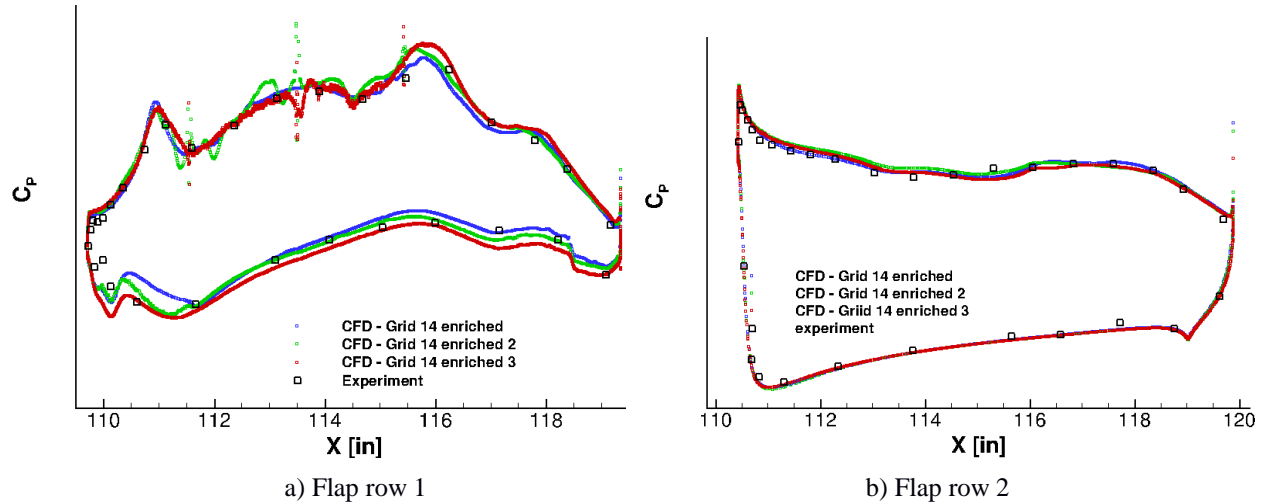


Figure 10. Time-averaged surface pressure distribution at flap inboard edge.

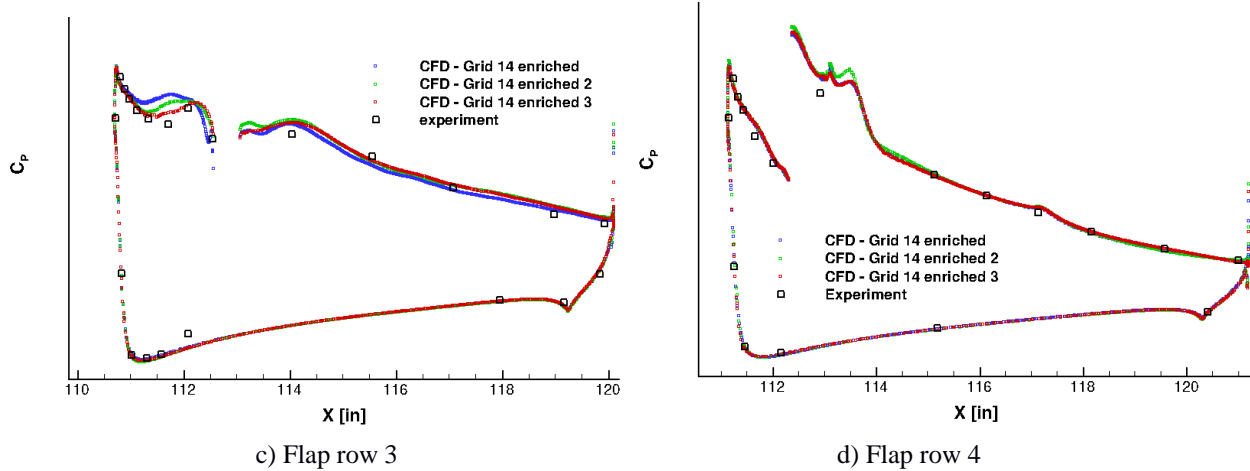


Figure 10. Concluded.

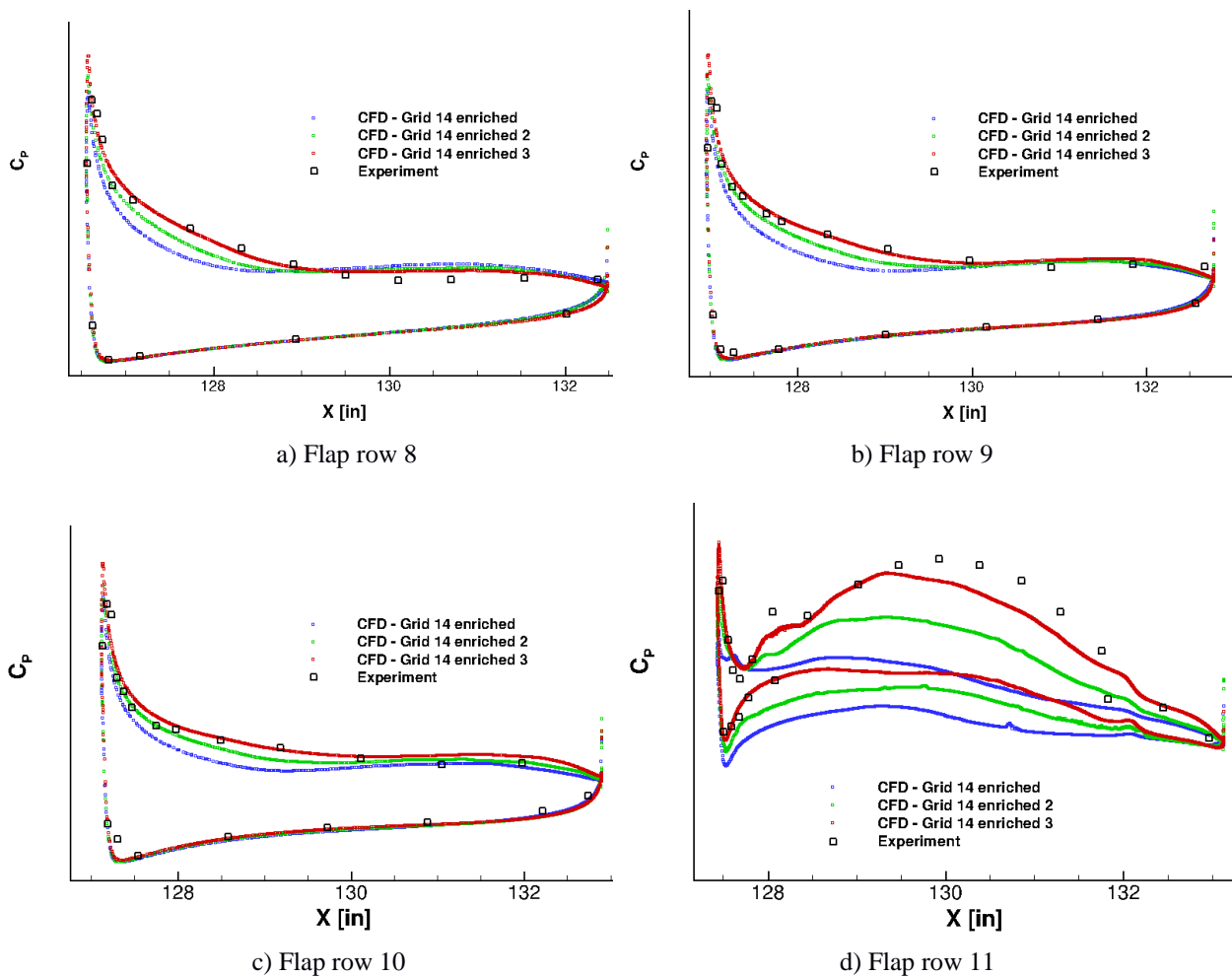


Figure 11. Time-averaged surface pressure distribution at flap outboard edge.

C. Surface Pressure Fluctuations

Accurate prediction of the surface pressure fluctuations in the vicinity of the flap side-edges is critical for a proper assessment of airframe noise source location. Analysis of the unsteady surface pressures from Grid 14 enriched

presented in KM indicated that the overall trends captured were encouraging. Yet, further improvement in some aspects of the computed solutions was still desired.¹⁵

a) *Inboard Tip*

Simulated power spectral density (PSD) values at probe locations on the upper surface near the flap inboard tip are shown in Fig. 12. At probes 67 and 1 (Figs. 12a and 12b, respectively), located closer to the leading-edge region (see Fig. 3), grid refinement improves the agreement with experiment across the frequency range, displaying a gradual reduction in the magnitude of the overprediction in the levels. At probe locations 2 (Fig. 12c) and 3 (Fig. 12d), located near the midchord region where the vortex on the side wall starts to spill over the upper surface, the effects of mesh refinement are minimal as no further improvement in the predicted levels or spectral shape is observed. However, for the other probes located between the midchord and trailing edge of the flap, spatial refinement yields a noticeable gain in the predicted pressure levels at all frequencies. In particular, at probes 5, 6, 7, and 9, grid refinement substantially improves the accuracy of the computed pressures for frequencies above 7 kHz.

The PSD plots for probes situated on the side-edge wall at the flap inboard tip are presented in Fig. 13. For probes 68 and 10 that are closer to the leading edge, there is now very good agreement between the simulated spectra obtained with Grid 14 enriched 3 and experimentally measured values up to 13–15 kHz, which is near the upper limit (16 kHz) of the operational range of the transducers installed on the semispan model. For probes 11 and 12, which are positioned along the path of the vortex on the side wall, grid refinement captures the spectral shapes much better and markedly extends the accuracy of the computed pressure fluctuations to frequencies beyond 7 kHz. Nevertheless, fluctuating pressure levels are still overpredicted, and in the case of probes 11 and 12, the overprediction is slightly worse. We must emphasize, however, that single-point surface measurements may not be the most reliable metric to assess the accuracy of the predicted pressures, as slight variations in the location of flow separation or reattachment on the side wall, caused by changes in spatial resolution, may have profound effects on surface pressures. As will be shown later, the farfield noise signature depends on the integrated effect of the fluctuating pressure field over the entire flap.

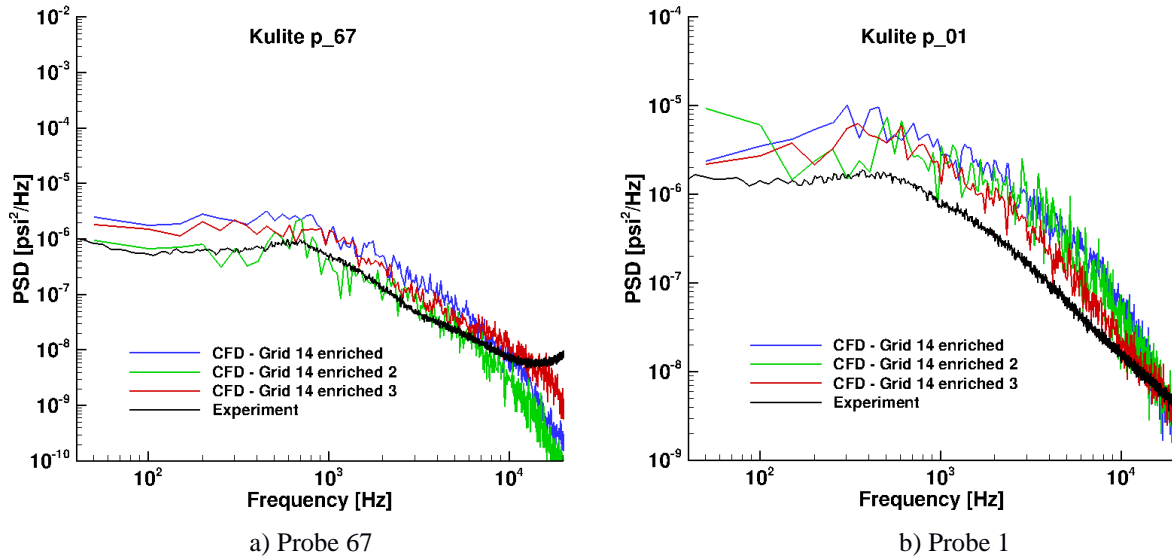
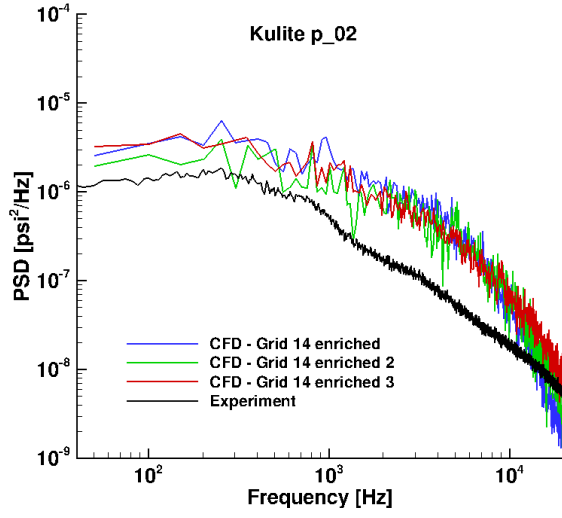
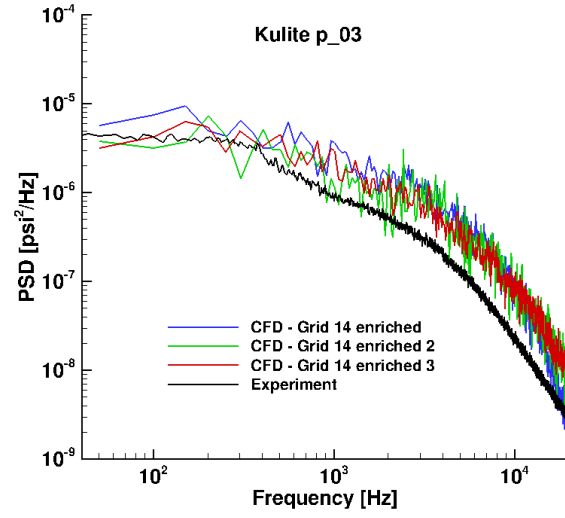


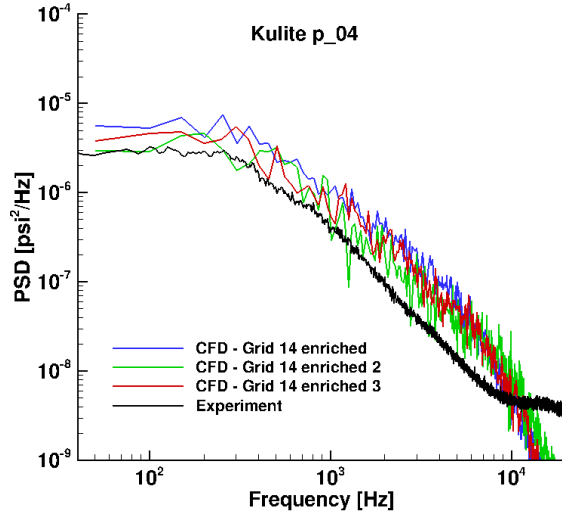
Figure 12. Power spectral density plots of pressure fluctuations on flap upper surface near inboard tip.



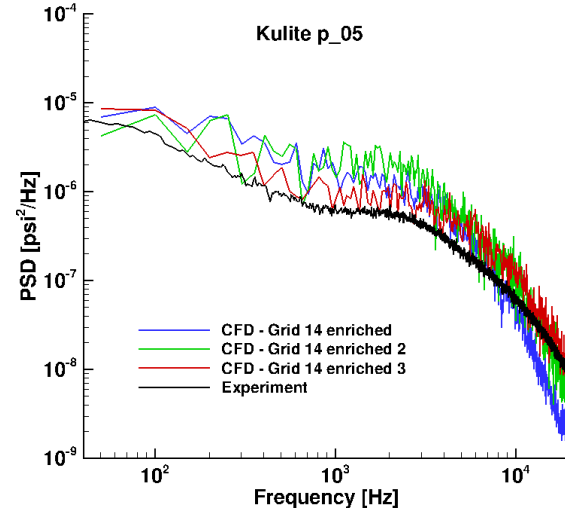
c) Probe 2



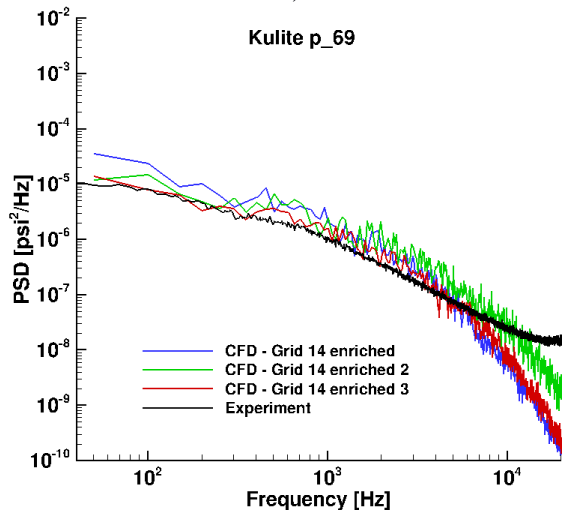
d) Probe 3



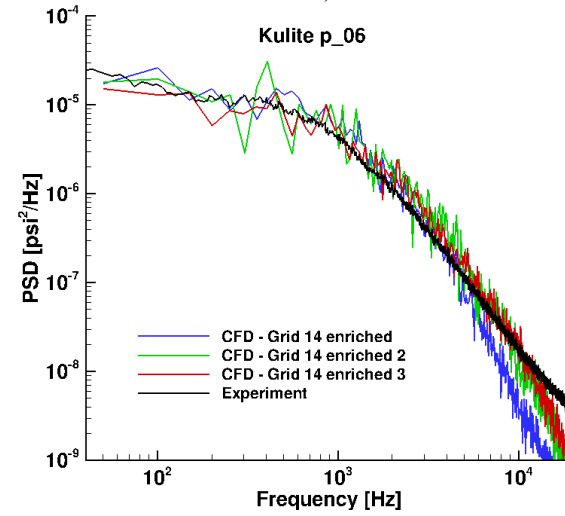
e) Probe 4



f) Probe 5

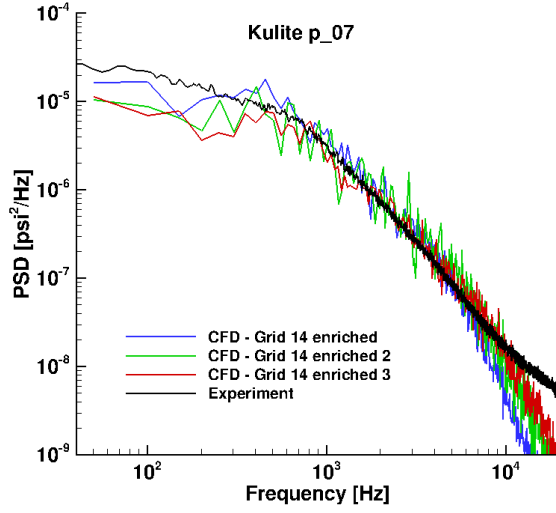


g) Probe 69

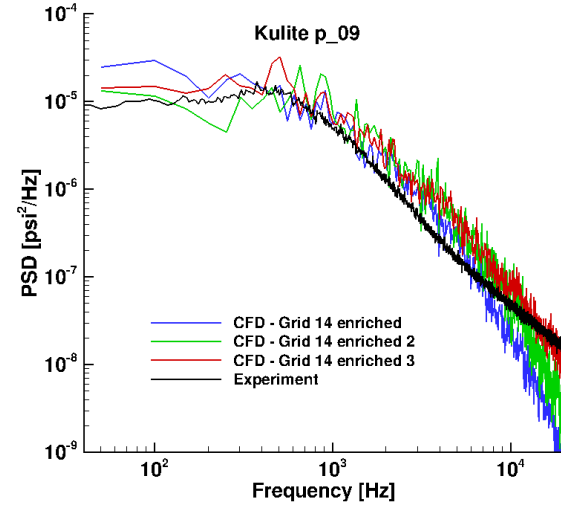


h) Probe 6

Figure 12. Continued.

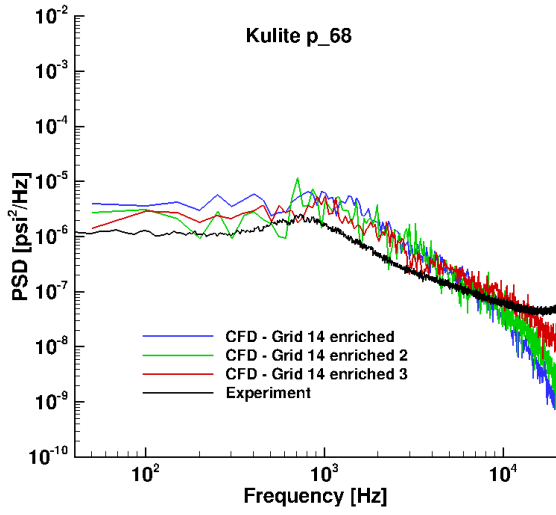


i) Probe 7

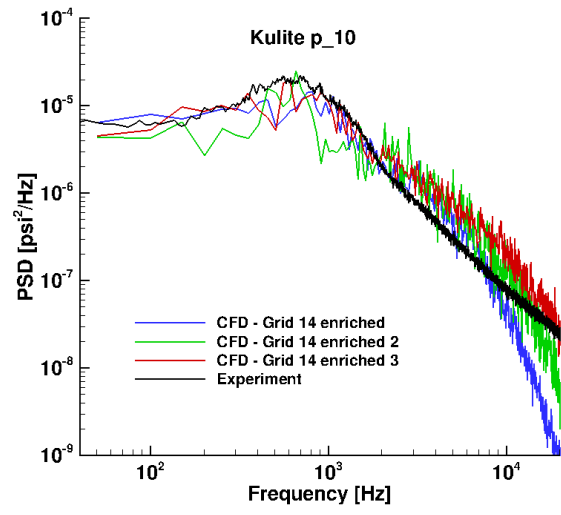


j) Probe 9

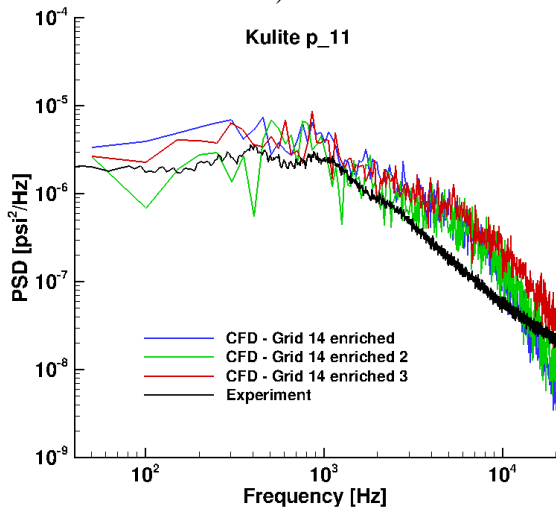
Figure 12. Concluded.



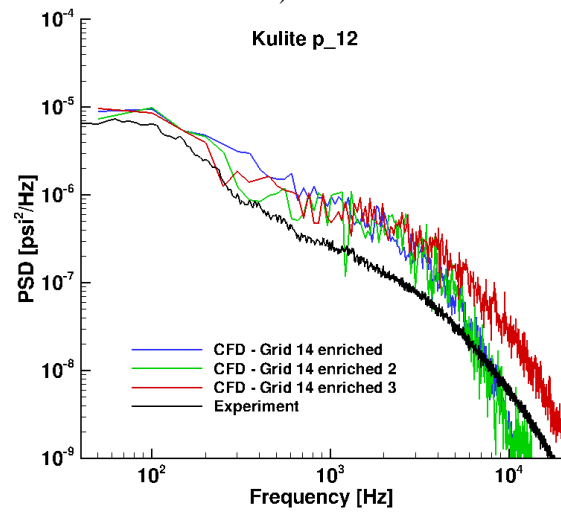
a) Probe 68



b) Probe 10



c) Probe 11



d) Probe 12

Figure 13. Power spectral density plots of pressure fluctuations on flap side-edge surface at inboard tip.

b) Outboard Tip

The simulated PSD distribution inside the cavity at the outboard side-edge is presented in Fig. 14. None of the simulated results agreed with the character of the measured data for frequencies below 500 Hz, which is prevalent for most probes positioned in the vicinity of the outboard tip. As indicated in KM (and discussed in the farfield noise section of this paper), most likely the low frequency behavior is influenced by the large zone of separated flow present over the outboard segment of the flap. The simulated time records span a small fraction of the measured data taken during tests of the 18%-scale model. Therefore, a plausible scenario is that the number of simulated cycles containing the low-frequency flow features is insufficient to allow the separated flow zone to reach its true time-periodic state. At higher frequencies, for the location closer to the flap leading edge (Fig. 14a), the baseline grid failed to predict the overall shape of the spectrum or to detect the cavity resonance near 6 kHz. The solution obtained with Grid 14 enriched 2 captures the resonance at a slightly higher frequency, but does not match the broadband character of the measured results at mid- and high-frequencies. In contrast, the spectrum obtained with Grid 14 enriched 3 shows a marked improvement relative to the other two solutions and captures both the cavity resonance and broadband character of the experimental results. Also note from Fig. 14a that the simulated cavity resonance is much more pronounced than that observed in the measured spectra. Most likely, this behavior is caused by subtle geometric differences between the tested and simulated models. One clear example of such differences is the representation and position of the bulb seal inside of the tip cavity. On the actual semispan model, the bulb seal was made of a soft foam and was hand-glued into the cavity. In contrast, the simulated seal is assumed to be rigid and its position inside the cavity was specified precisely. Farther downstream at probe 27 (Fig. 14b), improved spatial resolution yielded better agreement with measured data at higher frequencies, but also overprediction in pressure levels in the mid-frequency range.

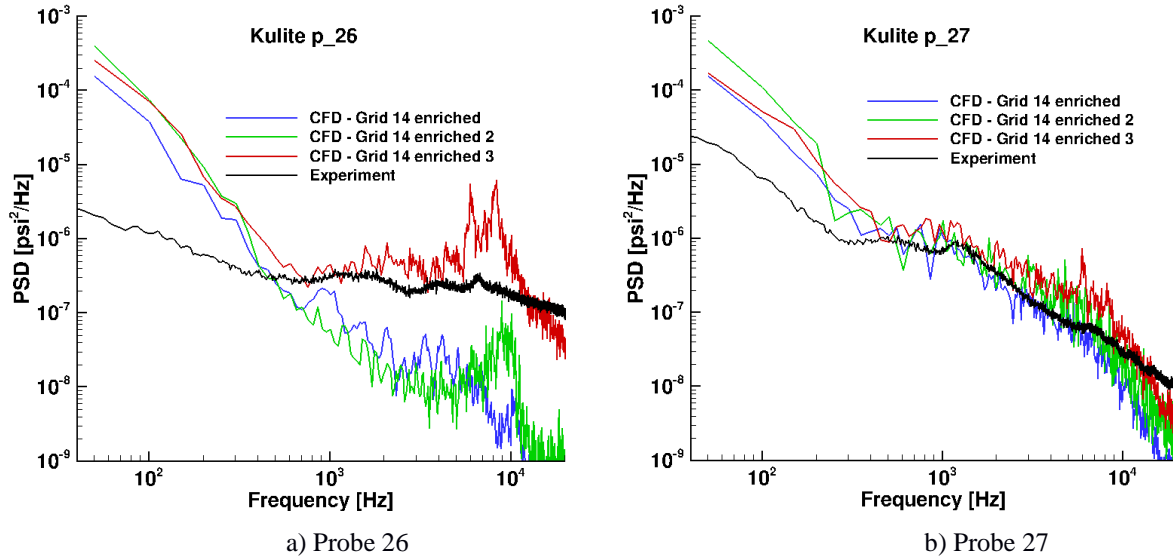
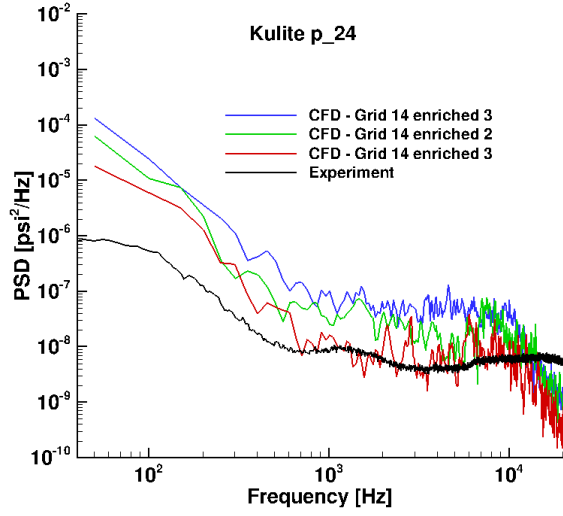
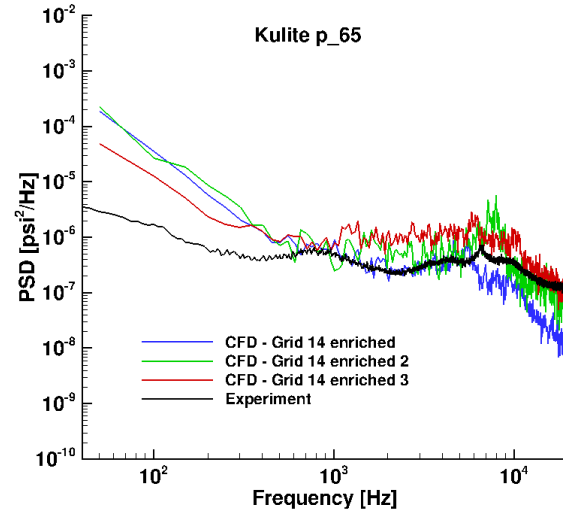


Figure 14. Power spectral density plots of the surface pressure in the outboard side-edge cavity.

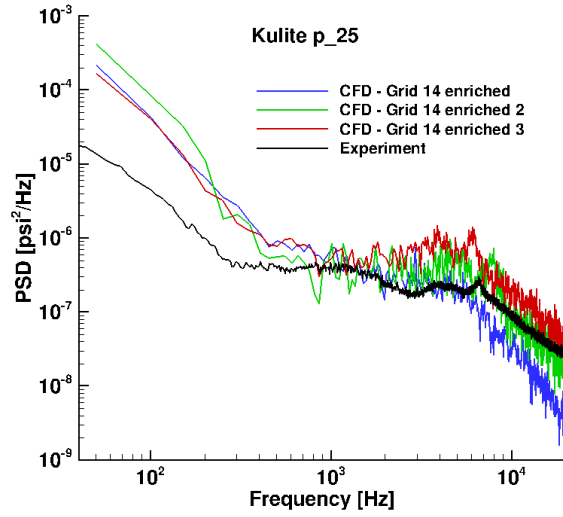
Simulated PSD values at various probe locations on the flap upper surface near the outboard side-edge are presented in Fig. 15. At most positions, spatial resolution refinement improves the agreement with measured data for frequencies above 600 kHz.



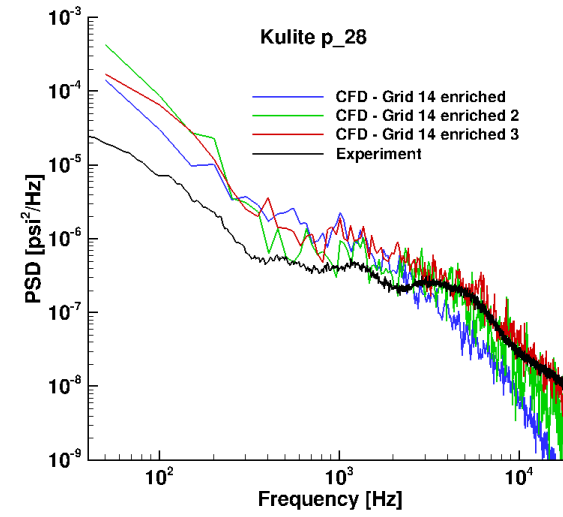
a) Probe 24



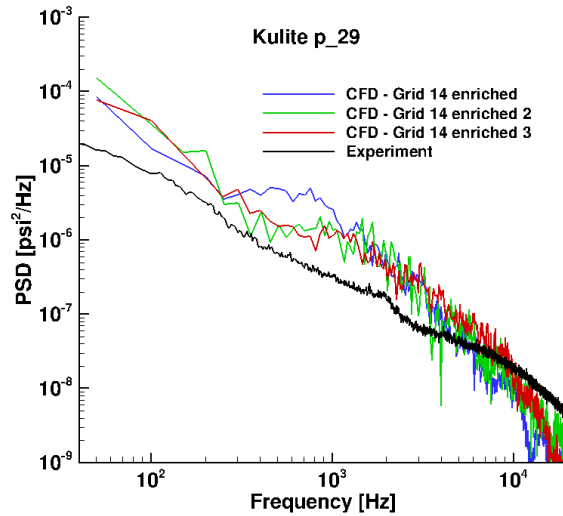
b) Probe 65



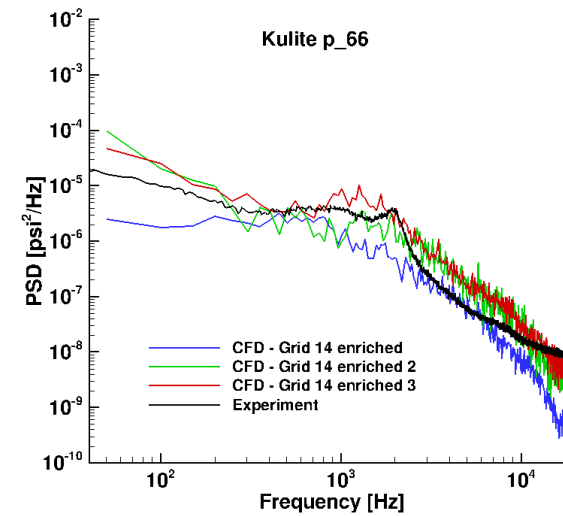
c) Probe 25



d) Probe 28



e) Probe 29



f) Probe 66

Figure 15. Power spectral density plots of pressure fluctuations on flap upper surface near outboard tip.

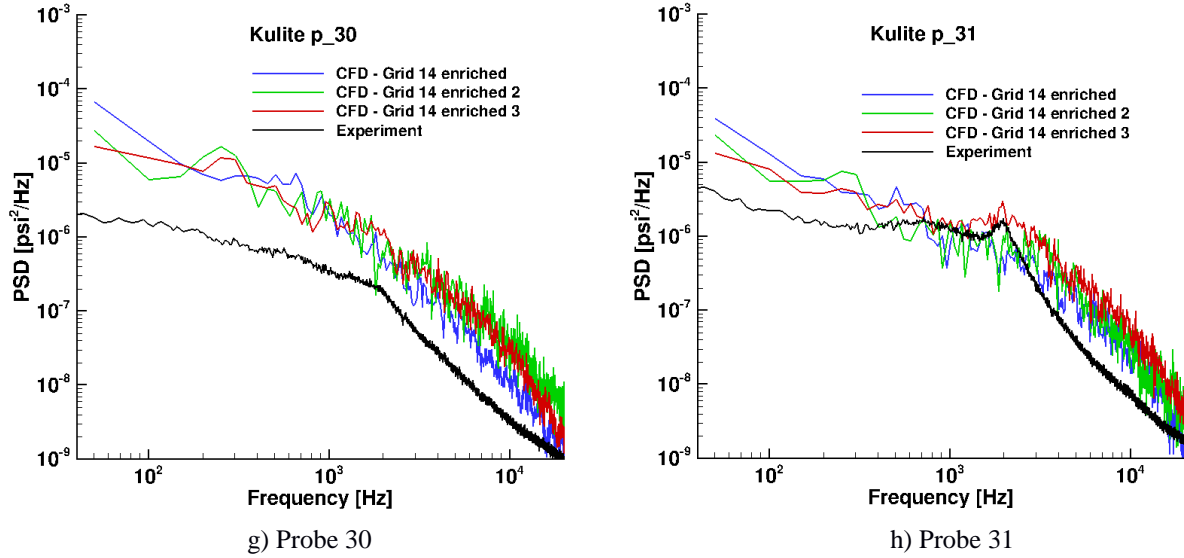


Figure 15. Concluded.

D. Farfield noise

The ultimate challenge and goal of the simulations is an accurate prediction of the farfield noise spectrum. The time history of the computed surface pressures was processed using a Ffowcs-Williams Hawking (FWH) propagation formulation to predict the noise at the overhead farfield point (92.02, 69.00, -195.00), which is 17.5 ft (5.334 m) away from the model. The resulting farfield noise spectrum is plotted in Fig. 16a, along with our earlier result and the measured PSD distribution. As seen in the figure, the simulated results for Grid 14 enriched failed to capture the cavity resonance and rolled off more rapidly than the measured spectrum for frequencies above 6 kHz. The noise spectrum obtained with Grid 14 enriched 3, with very refined node spacing at the outboard tip, captures the cavity resonance and agrees with measured results at higher frequencies up to 20 kHz. Notice that the simulated tonal component at the outboard edge cavity is stronger and occurs at lower frequencies relative to experiment. As mentioned earlier, this behavior can be attributed to differences in cavity geometry/volume caused by the bulb seal and instrumentation present in the tested model. Relative contributions to the farfield noise signature for the major components of the 18%-scale model aircraft are depicted in Fig. 16b. The black solid line was obtained from Grid 14 enriched 3 (Fig. 16a) with the surface pressure field from the entire model. The dash-dot line represents the farfield noise associated with the aircraft wing without the flap and the dashed line corresponds to the flap including its tracks and brackets. Figure 16b clearly demonstrates that for frequencies above 400 Hz, the fluctuating pressures on the flap surface are the primary sources determining the farfield noise footprint. At frequencies below 400 Hz, the wing contribution to the farfield noise is on par to that of the flap. However, we believe that the resemblance between the spectra at low frequencies indicates that the wing contribution is mostly caused by reflection of the sound waves that are actually produced by the flap. The prominent tone around 2,500 Hz in the wing spectrum results from two relatively small cavities present on the wing, adjacent to the outboard flap side edge.

To examine the spectral content of the noise produced by the flap, its surface was divided into three sections: two narrow strips adjacent to the inboard and outboard edges, respectively, and a segment containing the rest of the flap including the four brackets/tracks. The contributions of these three sections to the flap farfield noise spectrum are depicted in Fig. 17a. As expected, the inboard tip region is the more prominent source in the low- to mid-frequency (500 Hz – 3,000 Hz) range. For frequencies above 3 kHz, the spectral content is dominated by the contribution from the outboard tip. The remaining surfaces of the flap between the two narrow strips produce the sources that dominate the spectrum at low (sub 300 Hz) frequencies. This central segment also contributes substantially to the farfield noise signature in the 300 Hz – 3,000 Hz frequency range. To further explore where the low-frequency component of the farfield spectrum originates, the central segment of the flap was subdivided into four sections, each containing a flap bracket assembly. The contributions to the farfield noise from each section are shown in Fig. 17b. The figure clearly indicates that the low frequency component (sub 300 Hz) of the noise spectrum is associated with the flap sections identified as B, C, and D. Keep in mind, however, that the very low frequency segment of the spectrum may be affected by the shortness of the simulated time record.

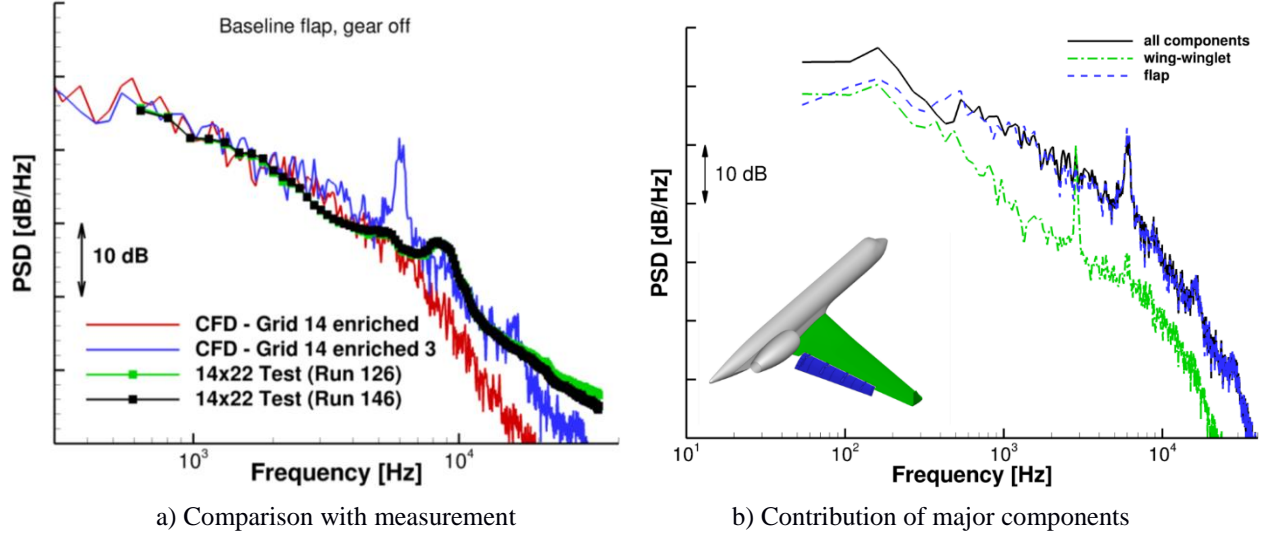


Figure 16. Power spectral density plots of the noise at the farfield point.

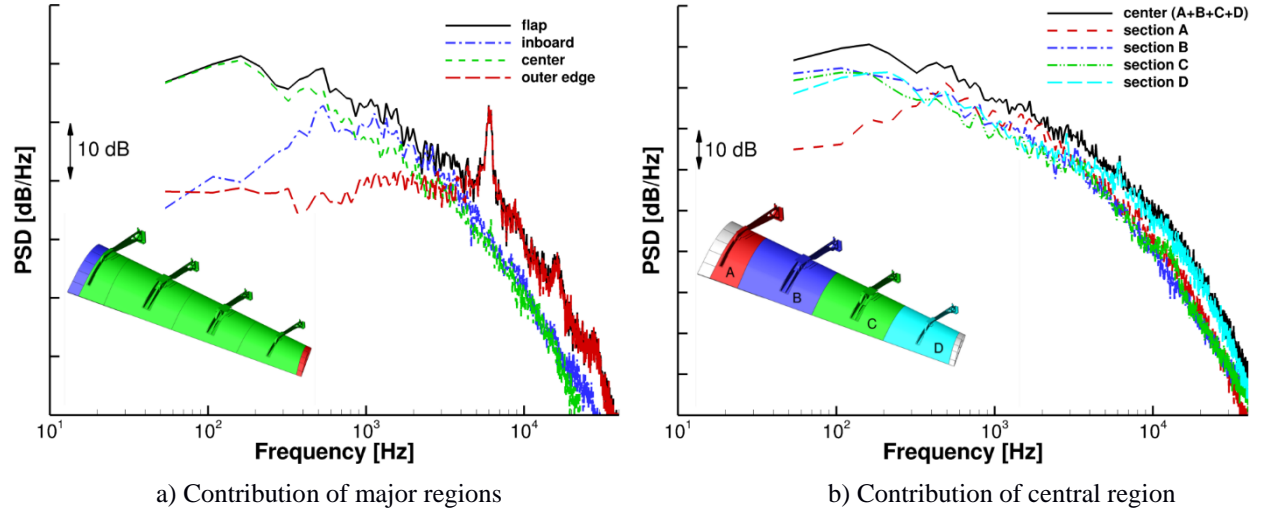


Figure 17. Flap surface segments used to identify farfield noise signature.

V. Concluding Remarks

Computational results from a spatial resolution study of flap tip flow and the effects on farfield noise signature for a high fidelity, 18%-scale, semispan model of a Gulfstream aircraft are presented in this paper. The current simulations were undertaken to determine the causes of deficiencies observed in our earlier computations of the same aircraft model. These deficiencies were observed mainly in the steady and unsteady surface pressures and off-surface flow field at the flap outboard tip area, where the presence of a cavity at the side-edge produces very complex flow features and interactions. In our earlier attempt, the discrepancies at the outboard edge were conjectured to be caused by insufficient spatial resolution; inability or inadequacy of the turbulence model to capture the complex, unsteady, three-dimensional flow; or a combination of both. The current simulations highlight the effects of spatial mesh refinements on the accuracy of the computed flow field.

The NASA FUN3D unstructured, compressible Navier-Stokes solver was used to perform the highly resolved, time-dependent, detached eddy simulations of the flow field surrounding the aircraft model. Starting with the grid used in our earlier simulations as a baseline, two additional grids with progressively finer mesh distributions in the vicinity of the model flap, in particular at the two tip regions, were developed. Comparison of the results obtained with the finest grid with wind tunnel measurements showed a marked improvement in the time-averaged surface pressure distribution at the outboard segment of the flap. The fluctuating surface pressure field also improved substantially with mesh refinement, resulting in better agreement with measured data at high frequencies. However,

the gain in accuracy was gradual and tended to be location-dependent, with some overprediction of the pressure levels observed in the earlier simulation still lingering.

When compared to measured data, the computed farfield noise spectrum in the overhead direction showed marked improvement in both broadband and tonal contents with spatial mesh refinement. The rapid roll-off at frequencies above 6 kHz observed in the solution obtained with the baseline grid was delayed to higher frequencies, yielding good agreement with the measured spectrum up to 18 – 20 kHz.

Despite the substantial reduction in cell size and the increased solution accuracy observed in this study, further gains in accuracy could be realized with additional mesh refinement. Whether further refinements are justified, given the computational cost of such an effort, depends on the flow quantity of interest. The observed spatial resolution trends amply demonstrate that the deficiencies reported in our previous computations are mostly caused by inadequate spatial resolution and are not related to the chosen turbulence model.

Acknowledgments

This work was partially supported by the Environmentally Responsible Aviation (ERA) and Flight Demonstrations and Capabilities (FDC) projects under the Integrated Aviation Systems Program (IASP) of NASA. The authors gratefully acknowledge Michael R. Wiese of Vigyan, Inc. for generating and refining the grids used during the computations. Our thanks also go to Scott Brynildsen, also of Vigyan, Inc., for providing geometry modifications and CAD support. Finally, all the simulations were performed on the Pleiades supercomputer at the NASA Advanced Supercomputing (NAS) facility at Ames Research Center. The logistical support provided by NAS staff is greatly appreciated.

References

- ¹Michel, U., Barsikow, B., Helbig, J., Hellmig, M., and Schüttelpelz, M., “Flyover Noise Measurements on Landing Aircraft with a Microphone Array,” AIAA Paper 98-2336, May 1998.
- ²Piet, J. F., Elias, G., and Lebigot, P., “Localization of Acoustic Sources from a Landing Aircraft with a Microphone Array,” AIAA Paper 99-1811, May 1999.
- ³Pott-Pollenske, M., Dobrzynski, W., Buchholz, H., Gehlhar, B., and Walle, F., “Validation of a Semiempirical Airframe Noise Prediction Method through Dedicated A319 Flyover Noise Measurements,” AIAA Paper 2002-2470, June 2002.
- ⁴Stoker, R., Guo, Y., Streett, C. L., and Burnside, N., “Airframe Noise Source Locations of a 777 Aircraft in Flight and Comparisons with Past Model Tests,” AIAA Paper 2003-3232, May 2003.
- ⁵Elkoby, R., Brusniak, L., Stoker, R., Khorrami, M. R., Abeyasinghe, A., and Moe, J. W., “Airframe Noise Results from the QTD II Flight Test Program,” AIAA Paper 2007-3457, May 2007.
- ⁶Khorrami, M. R., Lockard, D. P., Humphreys, Jr., W. M., Choudhari, M. M., and Van de Ven, T., “Preliminary Analysis of Acoustic Measurements from the NASA-Gulfstream Airframe Noise Flight Test,” AIAA Paper 2008-2814, May 2008.
- ⁷Horne, W. C., James, K. D., Arledge, T. K., Soderman, P. T., Burnside, N., and Jaeger, S. M., “Measurements of 26%-Scale 777 Airframe Noise in the NASA Ames 40- by 80-Foot Wind Tunnel,” AIAA Paper 2005-2810, May 2005.
- ⁸Jaeger, S. M., Burnside, N. J., Soderman, P. T., Horne, W. C., and James, K. D., “Microphone Array Assessment of an Isolated, 26%-Scale, High Fidelity Landing Gear,” AIAA Paper 2002-2410, June 2002.
- ⁹Khorrami, M. R., Hannon, J. A., Neuhart, D. H., Markowski, G. A., and Van de Ven, T., “Aeroacoustic Studies of a High-Fidelity Aircraft Model: Part 1-Steady Aerodynamic Measurements,” AIAA Paper 2012-2233, June 2012.
- ¹⁰Khorrami, M. R. and Neuhart, D. H., “Aeroacoustic Studies of a High-Fidelity Aircraft Model: Part 2- Unsteady Surface Pressures,” AIAA Paper 2012-2234, June 2012.
- ¹¹Khorrami, M. R., Humphreys, Jr. W. M., Lockard, D. P., and Ravetta, P. A., “Aeroacoustic Evaluation of Flap and Landing Gear Reduction Concepts,” AIAA Paper 2014-2478, June 2014.
- ¹²Neuhart, D. H., Hannon, J. A., and Khorrami, M. R., “Aerodynamic Measurements of a Gulfstream Aircraft Model with and without Noise Reduction Concepts,” AIAA Paper 2014-2477, June 2014.
- ¹³Yao, C.-S., Jenkins, L. N., Bartram, S. M., Harris, J., Khorrami, M. R., and Mace, W. D., “Flow-Field Investigation of Gear-Flap Interaction on a Gulfstream Aircraft Model,” AIAA Paper 2014-2479, June 2014.
- ¹⁴Khorrami, M. R., Fares, E., and Casalino, D., “Towards Full-Aircraft Airframe Noise Prediction: Lattice-Boltzmann Simulations,” AIAA Paper 2014-2481, June 2014.
- ¹⁵Khorrami, M. R. and Mineck, R. E., “Towards Full-Aircraft Airframe Noise Prediction: Detached Eddy Simulations,” AIAA Paper 2014-2480, June 2014.
- ¹⁶Vatsa, V., Lockard, D. P., and Khorrami, M. R., “Application of FUN3D Solver for Aeroacoustic Simulation of a Nose Landing Gear Configuration,” AIAA Paper 2011-2820, June 2011.

¹⁷Vatsa, V., Lockard, D. P., Khorrami, M. R., and Carlson, J.-R., “Aeroacoustic Simulation of a Nose Landing Gear in a Open-Jet Facility using FUN3D,” AIAA Paper 2012-2280, June 2012.

¹⁸Spalart, P. R. and Allmaras, S. R., “A One-Equation Turbulence Model for Aerodynamics Flows,” AIAA Paper 92-0439, 1992.

¹⁹Dacles-Mariani, J., Rogers, S., Kwak, D., Zilliac, G., and Chow, J., “A Computational Study of Wingtip Vortex Flowfield,” AIAA Paper 93-3010, July 1993.

²⁰Pirzadeh, S. Z., “Advanced Unstructured Grid Generation for Complex Aerodynamic Applications,” *AIAA Journal*, Vol. 48, No. 5, 2010, pp. 904–915.

²¹Pointwise® V17.2R2, <http://www.pointwise.com>, cited October 22, 2016.